



# First-principles predictions of qubits in defective MgS

Jijun Huang  and Xueling Lei \*

*Department of Physics, Jiangxi Normal University, Nanchang, Jiangxi 330022, China*



(Received 28 October 2021; revised 7 March 2022; accepted 24 May 2022; published 7 June 2022)

In this paper, MgS is evaluated to be a suitable qubit host material due to its wide bandgap, being nuclear spin free, and its weak spin-orbit coupling. The point defects including vacancies, substitutions, and defect pairs were systematically investigated using first-principles calculations. Results show that the neutral  $P_S V_{Mg}$  defect pair has  $C_{3v}$  symmetry with the defect level sequence of  $E_1 > E_{exy} > E_2$ . In addition, the net spin and defect levels of  $P_S V_{Mg}$  can be tuned by charge states. The  $P_S V_{Mg}^{2+}$  and  $P_S V_{Mg}^{2-}$  defects are relatively stable with the charge transition level of  $\sim 2.53$  eV. The four charged defect states of  $P_S V_{Mg}^+$ ,  $P_S V_{Mg}^{2+}$ ,  $P_S V_{Mg}^-$ , and  $P_S V_{Mg}^{2-}$  may be plausible qubits with nonzero spin, and their zero-phonon lines indicate the corresponding fluorescence wavelengths fall within the infrared band. Furthermore, the zero field splitting of the  $P_S V_{Mg}^+$  and  $P_S V_{Mg}^-$  shows that the values of parameter  $D$  are in the range of microwaves. The hyperfine constants are roughly proportional to the spin difference charge density and exponentially decay as a function of the distance from the P site.

DOI: [10.1103/PhysRevB.105.224104](https://doi.org/10.1103/PhysRevB.105.224104)

## I. INTRODUCTION

Understanding the physics of point defects in semiconductors is of outstanding importance for controlling their optical and electrical properties [1,2]. In recent years, considerable efforts have been made to study point defect quantum bits (qubits) in semiconductors, including single or ensemble isolated qubits for their applications in a broad range of physical systems such as quantum information processing [3,4], quantum computation [5–8], spintronics [9], and quantum sensors [10,11]. For instance, the qubit can be used as an atomic-scale sensor for the measurement of temperature [12,13], electric field [14], strain [15], and other physical quantities. Moreover, active point defect qubits can act as a single photon source [16,17] or a qubit [9,18,19]. It is known that the famous qubit is the negatively charged nitrogen-vacancy color center in diamond ( $NV^-$ ), formed by a carbon vacancy and a substitutional nitrogen atom next to the vacancy. The  $NV^-$  color center has decent spin properties but suffers from very poor optical characteristics. For example, the electron spin of the  $NV^-$  color center can be effectively manipulated and measured by microwave and optical pump methods [19–21]. However, the  $NV^-$  color center only emits  $\sim 4\%$  fluorescence into the zero-phonon line (ZPL), which greatly limits its use for quantum information processing without photonic cavities or other photonic structures [22]. In contrast, the negatively charged silicon-vacancy color center in diamond ( $SiV^-$ ) emits  $\sim 80\%$  photons into the ZPL, with spectral stability and narrow inhomogeneous distribution, which makes the  $SiV^-$  color center an ideal building block for a distributed quantum network [23–26]. In addition to the leading  $NV^-$  and [27–29]  $SiV^-$  color centers [30–35] in diamond, other defect centers have been proposed as candidate qubits, such as GeV [36,37] and SnV centers in diamond [38];  $N_C V_{Si}^-$  [39],  $Al_{Si} V_C$  [40],

and  $V_C V_{Si}$  [41–43] in SiC;  $V_{Ga} O_N$  and  $Ni_{Ga} V_N$  centers in GaN [44–46]; and the  $V_B O_N$  center in cubic boron nitride (c-BN) [47].

Generally, for a good qubit system, the point defects should satisfy the requirements that the defect levels must be located in the bandgap of the host material and allowed internal excitation without interference of the bulk valence-band and conduction-band states. Moreover, a more accurate requirement of a qubit system would be the orbital multiplets, i.e., an energy splitting must exist between at least two of the spin sublevels. If the qubit state is to be manipulated, this energy splitting should fall within an appropriate range of the frequency spectrum. Specifically, a qubit with spin triplets can be easily realized by microwave manipulation. On the other hand, the host materials should fulfill the requirements of high-quality bulk or thin film single crystals, wide bandgap semiconductors, weak spin-orbit coupling (SOC), and the constituent elements with no net nuclear spin [48,49]. Of these, the weak SOC and zero nuclear spin can increase individual qubit state lifetimes to allow for operations and readout.

Undoubtedly, it is worthwhile to identify the potential color centers in semiconductors that meet the above requirements for building solid-state quantum systems. Magnesium sulfide is a wide bandgap semiconductor, and its structure is like that of diamond. Therefore, we hope to find a potential color center in MgS, like  $NV^-$  or  $SiV^-$  color centers in diamond. In this paper, we have performed a systematic study of the electronic structure and defect levels of single point defects and defect pairs in MgS with full atomic relaxations and presented a comprehensive physical understanding of point defects. Our calculations suggest that the  $P_S V_{Mg}$  defect in different charge states may be plausible qubits.

## II. COMPUTATIONAL DETAILS

All first-principles calculations in this paper were carried out using the Vienna *Ab initio* Simulation Package

\*xueling@mail.ustc.edu.cn

(VASP) [50,51]. The projector augmented wave pseudopotentials [52,53] describe the interaction between the core and the valence electron, and the generalized gradient approximation parametrized by Perdew-Burke-Ernzerhof (PBE) [54] is used to calculate the electron exchange and correlation energies. Atomic positions and lattice constants of all systems were fully optimized under the total energy convergence criteria of  $1 \times 10^{-5}$  eV and the force convergence criteria of  $0.01$  eV  $\text{\AA}^{-1}$ . The phonon spectrum of MgS was calculated using a primitive cell with two atoms by the PHONOPY code [55] implemented in VASP. The Monkhorst-Pack k-point mechanism [56] was used, and the k-point densities for MgS primitive cell and supercell optimization were  $0.04/\text{\AA}$  and  $0.03/\text{\AA}$ , respectively. A 400 eV cutoff was set to the plane-wave basis expansion. For the calculations of density of states, the Gaussian smearing method in combination with a small SIGMA of 0.05 was used. In addition, the Heyd-Scuseria-Ernzerhof (HSE) hybrid exchange-correlation functional has been used to accurately calculate the electronic structure of the MgS primitive cell for comparison with experimental values and charged defect pairs in a  $2 \times 2 \times 2$  MgS supercell with 64 atoms, where the ratio of Hartree-Fock exchange term used the default value of 0.25.

To evaluate the stability of defects, the defect formation energy ( $E_{\text{form}}$ ) was defined as

$$E_{\text{form}}[V_X] = E_{\text{defective}} - E_{\text{perfect}} + \mu_X, \quad (1)$$

$$E_{\text{form}}[Y_S] = E_{\text{defective}} - E_{\text{perfect}} + \mu_S - \mu_Y, \quad (2)$$

$$E_{\text{form}}[P_S V_{Mg}] = E_{\text{defective}} - E_{\text{perfect}} + \mu_{MgS} - \mu_P, \quad (3)$$

$$E_{\text{form}}[P_S V_{Mg}^q] = E_{\text{total}}[P_S V_{Mg}^q] - E_{\text{total}}[\text{bulk}] + \mu_{MgS} - \mu_P + q(\Delta\varepsilon_F + \varepsilon_{VBM}^{\text{bulk}} + \Delta V), \quad (4)$$

where  $E_{\text{defective}}$  and  $E_{\text{perfect}}$  are the total energy of MgS with and without defects,  $\mu_X$  ( $X = \text{Mg}$  or  $\text{S}$ ) and  $\mu_Y$  ( $Y = \text{N}, \text{O}, \text{F}, \text{P}, \text{Cl}, \text{As}, \text{and Se}$ ) are the chemical potentials of the corresponding atoms, and  $\mu_{MgS}$  is the energy of a pair of MgS atoms calculated from perfect MgS crystal. Here,  $E_{\text{total}}[P_S V_{Mg}^q]$  and  $E_{\text{total}}[\text{bulk}]$  are the total energies of the supercell with  $P_S V_{Mg}$  defects in charge state  $q$  and the perfect crystal supercell without any defect, respectively. Also,  $\Delta\varepsilon_F$  changes within the bandgap,  $\varepsilon_{VBM}^{\text{bulk}}$  is the energy of the valence band maximum (VBM), and  $\Delta\varepsilon_F + \varepsilon_{VBM}^{\text{bulk}}$  represents the Fermi level of MgS bulk. The correction term  $\Delta V$  is used to align the electrostatic potential between the defect supercell and the perfect bulk.

### III. RESULTS AND DISCUSSION

#### A. Structural and electronic properties of MgS

Like the structure of diamond, the MgS semiconductor with  $F\bar{4}3m$  space group (No. 216) has face-centered cubic (fcc) structure. The optimized MgS primitive cell is shown in Fig. 1(a), from which one can see that each S or Mg atom coordinates with four Mg or S atoms, forming a tetrahedron. The electronic structures of MgS calculated by accurate hybrid density functional HSE06 are shown in Fig. 1(b). Both

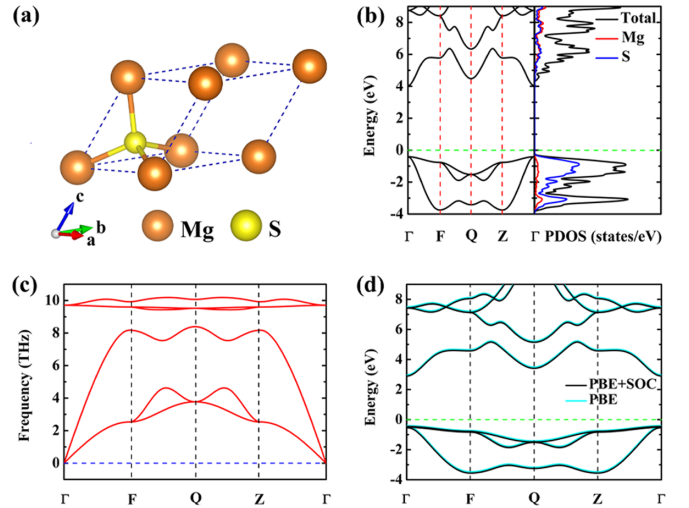


FIG. 1. (a) Structure, (b) electronic properties, (c) phonon spectrum, and (d) band structures of MgS without and with spin-orbit coupling (SOC) of MgS primitive. The electronic properties were calculated at the HSE06 level and the SOC calculated at the PBE level.

the VBM and the conduction band minimum (CBM) are at the  $\Gamma$  point, suggesting that MgS is a direct bandgap semiconductor. The calculated bandgap is 4.44 eV, which compares extremely well with the experimental gap of 4.45 eV [57,58] and is larger than that of typical semiconductor GaN (3.28 eV) [45]. In addition, to examine the stability of MgS, phonon dispersion spectroscopy has been conducted. As shown in Fig. 1(c), clearly, there are no imaginary frequencies in the phonon spectrum, indicating that the MgS semiconductor is dynamically stable. To examine the SOC intensity in the MgS semiconductor, the energy band structures have been calculated with the SOC. Figure 1(d) shows the band structures of MgS without and with SOC calculated at the PBE level. The SOC in MgS is fairly weak. All these results indicate that the MgS crystal looks like a promising host material for the qubit system.

#### B. Structural and electronic properties of a single point defect in MgS

Since MgS has weak SOC and is a wide bandgap semiconductor, it can be used as a potential qubit host material. To investigate the point defect in the MgS semiconductor, we construct the MgS supercell with 64 atoms. Here, two types of point defects are considered: vacancy defects including Mg vacancy ( $V_{Mg}$ ) and S vacancy ( $V_S$ ) and impurity defects including N, O, F, P, Cl, As, and Se substitutions. The vacancy defects can be created by removing one Mg or S atom from its lattice site in the perfect system, and the impurity defects are created by replacing the S atom by N, O, F, P, Cl, As, and Se atoms (denoted as  $N_S, O_S, F_S, P_S, Cl_S, As_S,$  and  $Se_S$ , respectively). The schematic diagram of each point defect configuration in a  $2 \times 2 \times 2$  MgS supercell is shown in Fig. 2, and then the defect formation energies and the defect levels of individual point defects have been studied.

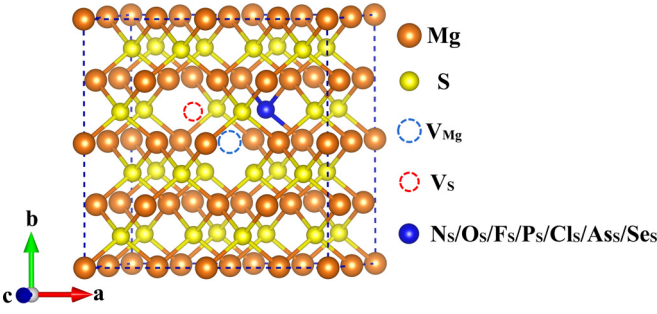


FIG. 2. Schematic diagram of each point defect configuration in a  $2 \times 2 \times 2$  MgS supercell.

Based on the symmetry of the MgS crystal structure, there is only one kind each of  $V_{Mg}$  and  $V_S$  defects. The configurations along with the corresponding electronic structures are shown in Fig. S1 in the Supplemental Material [59].  $V_{Mg}$  and  $V_S$  can cause spin-polarization and spin-nonpolarization defect states in the bandgap of MgS, respectively. Furthermore, it can be found from Fig. S1(b) in the Supplemental Material [59] that the spin-up defect states are very close to the VBM, and the spin-down defect states split into two small peaks around the Fermi level.

For the impurity defects, seven impurity atoms have been considered in this paper. The schematic diagram of configurations for  $N_S$ ,  $O_S$ ,  $F_S$ ,  $P_S$ ,  $Cl_S$ ,  $As_S$ , and  $Se_S$  defects and the corresponding electronic structures are shown in Fig. S2 in the Supplemental Material [59]. Of these defects,  $O_S$ ,  $F_S$ ,  $Cl_S$ , and  $Se_S$  cause spin nonpolarization, whereas  $N_S$ ,  $P_S$ , and  $As_S$  cause spin polarization. The first-principles results show that the  $P_S$  and  $As_S$  defects have four defect levels in the bandgap of MgS, respectively. Two spin-up levels are under the Fermi level, and two spin-down levels locate on both sides of the Fermi level. Thus, for the spin-down electrons in the  $P_S$  and  $As_S$  defects, the electron transition from occupied defect states to the unoccupied defect states can be realized. Thus, the neutral  $P_S$  and  $As_S$  point defects in MgS seem to be potential candidate qubits.

To evaluate the stability of vacancy defects and impurity defects, the defect formation energies of  $V_{Mg}$ ,  $V_S$ ,  $N_S$ ,  $O_S$ ,  $F_S$ ,  $P_S$ ,  $Cl_S$ ,  $As_S$ , and  $Se_S$  point defects were estimated according to the formulas in Eqs. (1) and (2) described in computational details, in which the chemical potential references of the elements were using atomic energies defined based on Mg- or S-rich conditions. Referring to Ref. [40], under Mg-rich conditions,  $\mu_{Mg}$  is calculated from magnesium metal, and  $\mu_S = \mu_{MgS} - \mu_{Mg}$ . Under S-rich conditions,  $\mu_S$  is calculated from bulk sulfur, and  $\mu_{Mg} = \mu_{MgS} - \mu_S$ . From the definition of defect formation energy, the smaller the defect formation energy, the more stable the defect, and then the corresponding defect concentration should be higher. The for-

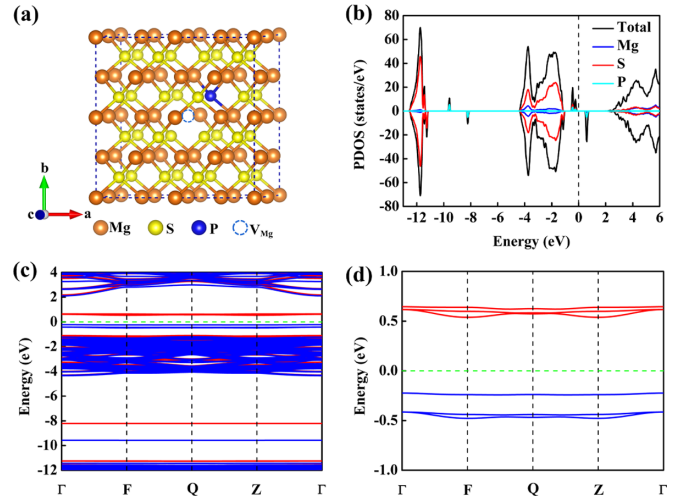


FIG. 3. (a) Configuration of the  $P_S V_{Mg}$  defect in MgS, (b) the corresponding projected density of states (PDOS), (c) the band structure, and (d) the amplified band structure with an energy range of  $-1.0$  to  $1.0$  eV. The two channels of spin-up and spin-down states are marked by blue and red lines, respectively.

mation energies of these defects are summarized in Table I, from which we can see that  $V_{Mg}$  has lower formation energy than  $V_S$  under S-rich conditions, indicating that the concentration of  $V_{Mg}$  defects may be higher than that of  $V_S$  defects. On the contrary, under Mg-rich conditions, the concentration of  $V_S$  defects may be higher than that of  $V_{Mg}$  defects due to its lower formation energy. In addition, the formation energy of  $P_S$  defects is slightly lower than that of  $As_S$  defects under both Mg- and S-rich conditions, indicating that the  $P_S$  defects are easier to form than the  $As_S$  defects in MgS crystal. Therefore, the P impurity atom has been chosen in the next defect pair calculations.

### C. Structural and electronic properties of a defect pair in MgS

Now we turn to investigations of defect pairs in MgS. Since there are spin-polarized defect states in the  $V_{Mg}$  and  $P_S$  defects, a defect pair consisting of a Mg vacancy and an adjacent substitutional P impurity on a S site has been constructed, denoted as  $P_S V_{Mg}$ , and the configuration of the  $P_S V_{Mg}$  defect pair in MgS is shown in Fig. 3(a). According to the formula in Eq. (3) described in computational details, the formation energy of the  $P_S V_{Mg}$  defect is calculated to be 5.24 eV. On the other hand, we also constructed the second neighbor defect model, where  $V_{Mg}$  and  $P_S$  are the second nearest neighbors, as shown in Fig. S3 in the Supplemental Material [59]. The optimized results show that the energy of the second neighbor model is 1.24 eV higher than that of the first neighbor model, indicating that  $V_{Mg}$  and  $P_S$  tend to form a  $P_S V_{Mg}$  defect pair. As seen from Fig. 3(b), there are one spin-up ( $-9.58$  eV) and

TABLE I. The formation energies of  $V_{Mg}$ ,  $V_S$ ,  $N_S$ ,  $O_S$ ,  $F_S$ ,  $P_S$ ,  $Cl_S$ ,  $As_S$ , and  $Se_S$  point defects under Mg- or S-rich conditions.

Point defects	$V_{Mg}$	$V_S$	$N_S$	$O_S$	$F_S$	$P_S$	$Cl_S$	$As_S$	$Se_S$
$E_{form}$ Mg-rich	6.10	1.38	0.96	-4.56	-3.21	0.54	-2.65	0.62	-2.61
$E_{form}$ S-rich	2.53	4.95	4.52	-0.99	0.36	4.10	0.92	4.19	0.96

one spin-down ( $-8.22$  eV) electronic states in deep levels, and there are occupied spin-up and unoccupied spin-down electronic states in the bandgap of MgS. With further observation, we found that there are two peaks next to each other for the occupied states; the left peak is higher, while the right peak is lower. This indicates that the left peak has degenerate states. Similarly, the unoccupied states also are degenerate states due to the higher peak. Moreover, these defect states are mainly contributed by impurity phosphorus atoms. Figure 3(c) shows the corresponding band structures, where the blue and red lines represent spin-up and spin-down states, respectively. To go further, the amplified band structures with an energy window of  $-1.0$  to  $1.0$  eV are shown in Fig. 3(d), from which we can see that there are six defect levels in the bandgap of MgS, that is, three occupied spin-up and three unoccupied spin-down levels. The lower spin-up level is double degenerate. The spin-down levels split into two groups, and the lower is also double degenerate. In addition, we performed test calculations of the defect concentration. As Fig. S4 in the Supplemental Material [59] shows, the  $P_S V_{Mg}$  defect pair in a  $4 \times 4 \times 4$  MgS supercell with 512 atoms has been fully optimized; the defect levels are consistent with those in a 64-atom supercell. Additionally, the bandgap of the  $P_S V_{Mg}$  defect in MgS is  $0.87$  eV in a 64-atom supercell and  $0.82$  eV in a 512-atom supercell calculated at the PBE level, showing that the size of the supercell does not affect the electronic structure of the  $P_S V_{Mg}$  defect. This indicates that the 64-atom model used in this paper is suitable, and the results are reliable.

Generally, the molecular orbitals of vacancy-related defects with  $C_{3v}$  symmetry consist of a linear combination of four orbitals of atoms nearest to the vacancy. For example, for the case of the  $P_S V_{Mg}$  defect pair, four atomic orbitals include one  $sp^3$  orbital of the P atom ( $\vartheta_0$ ) and three  $sp^3$  orbitals of the S atoms ( $\vartheta_1, \vartheta_2, \vartheta_3$ ) pointing to the  $V_{Mg}$  vacancy. The first-principles calculations show that the length of the S-S bonds between the three nearest S atoms equals  $\sim 3.9$  Å, and the length of the three S-P bonds is  $\sim 3.0$  Å, which indicates that the  $P_S V_{Mg}$  defect has  $C_{3v}$  symmetry. According to the group theory analysis, the irreducible representation of  $C_{3v}$  symmetric group has two  $a_1$  and two  $e$  molecular orbitals [60]:

$$a_1(1) = \frac{1}{\sqrt{3}S_1}(\vartheta_1 + \vartheta_2 + \vartheta_3 - 3\lambda\vartheta_0), \quad (5)$$

$$a_1(2) = \vartheta_0, \quad (6)$$

$$e_x = \frac{1}{\sqrt{3}S_2}(2\vartheta_3 - \vartheta_1 - \vartheta_2), \quad (7)$$

$$e_y = \frac{1}{S_2}(\vartheta_1 - \vartheta_2), \quad (8)$$

where  $S_1 = \sqrt{1 + 2\eta - 3\lambda^2}$ ,  $S_2 = \sqrt{2 - 2\eta}$ ,  $\eta = \langle \phi_1 | \phi_2 \rangle$ , and  $\lambda = \langle \phi_P | \phi_1 \rangle$ . For simplicity, we ignore the overlap between atomic orbitals, that is,  $\eta = \lambda = 0$ . The corresponding energies of these molecular orbitals are

$$E_1 = \langle a_1(1) | H | a_1(1) \rangle \approx \alpha + 2\beta, \quad (9)$$

$$E_2 = \langle a_1(2) | H | a_1(2) \rangle \approx \alpha_0, \quad (10)$$

$$E_{ex} = E_{ey} = \langle e_x | H | e_x \rangle = \langle e_y | H | e_y \rangle \approx \alpha - \beta, \quad (11)$$

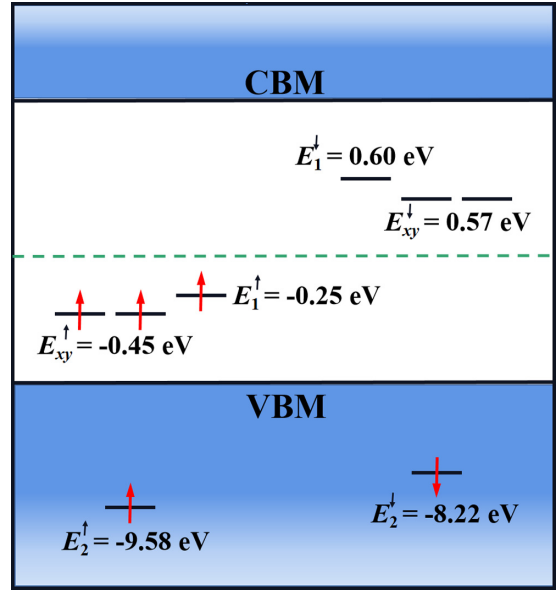


FIG. 4. The schematic diagram of defect energy levels sequence. The red arrow represents the occupied states, and the two channels of spin-up and spin-down states are marked by up and down arrows, respectively.

where  $\alpha_0 = \langle \phi_0 | H | \phi_0 \rangle$ ,  $\alpha = \langle \phi_i | H | \phi_i \rangle$  ( $i = 1, 2, 3$ ), and  $\beta = \langle \phi_i | H | \phi_j \rangle$  ( $i, j = 1, 2, 3, i \neq j$ ). Here, the transfer term  $\beta$  is determined by the type of vacancy defect. It is positive for cation vacancy-related defects and negative for anion vacancy-related defects [61]. For the  $P_S V_{Mg}$  defect, the double degenerate levels  $E_{exy}$  are lower than single-level  $E_1$  due to the positive value of  $\beta$ , that is,  $E_{exy} < E_1$ . On the other hand, the electronegativity of the  $sp^3$  orbitals of the P atom is much larger than that of the  $sp^3$  orbitals of the S atoms, so the energy of the  $a_1(2)$  molecular orbital formed by the  $sp^3$  orbitals of the P atom is lower than that of the  $a_1(1)$  molecular orbital formed by mixed  $sp^3$  orbitals of S and P atoms, that is,  $E_2 < E_1$ . Therefore, the group theory analysis is consistent with the defect-level calculations.

Based on group theory analysis and first-principles calculations, the arrangement order of defect levels in the  $P_S V_{Mg}$  defect is identified:  $E_1 > E_{exy} > E_2$ . As shown in Fig. 4, both  $E_1$  and  $E_{exy}$  levels are in the bandgap of MgS, while the  $E_2$  level appears in the deep valence bands. It should be noted that the degenerate energy levels  $E_{exy}$  are lower than the single energy level  $E_1$  in the  $P_S V_{Mg}$  defect. This is not in agreement with the defect levels of the  $NV^-$  center in diamond, where the degenerate levels  $E_{exy}$  are the highest levels [62]. Figure 4 further shows that there are three unpaired electrons to occupy the  $E_{xy}^{\uparrow}$  and  $E_1^{\uparrow}$  levels, whereas the  $E_{xy}^{\downarrow}$  and  $E_1^{\downarrow}$  levels are empty, then resulting in the quartet ground state. Therefore, the net spin of the  $P_S V_{Mg}$  defect is  $S = \frac{3}{2}$ , and the local magnetic moment is  $3 \mu_B$ .

To verify the defect energy level sequence, we carried out calculations of the partial charge density of molecular orbitals in the  $P_S V_{Mg}$  defect in the order of energy from high to low, as shown in Fig. 5. Obviously, the charge density of  $a_1(1)$  and

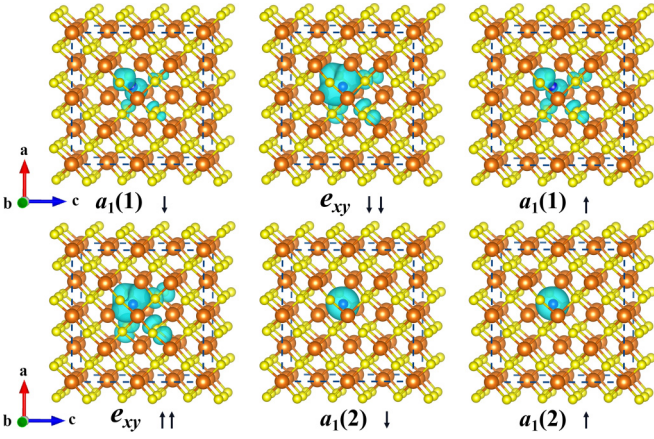


FIG. 5. The partial charge density of molecular orbitals in the  $P_S V_{Mg}$  defect in the order of energy from high to low. The isosurface value is  $2 \times 10^{-3} e/\text{\AA}^3$ . The two channels of spin-up and spin-down states are marked by up and down arrows, respectively.

$e_{xy}$  orbitals is dominantly on the P and three S atoms, indicating that the molecular orbitals of  $a_1(1)$  and  $e_{xy}$  consist of  $\emptyset_0, \emptyset_1, \emptyset_2,$  and  $\emptyset_3$  atomic orbitals. On the contrary, the charge density of the  $a_1(2)$  orbital is only distributed on the P atom, suggesting that the molecular orbitals of  $a_1(2)$  only consist of the  $\emptyset_0$  atomic orbital. On the other hand, the charge density of  $e_{xy}$  is distinct larger than that of  $a_1(1)$ , which indicates that the  $e_{xy}$  molecular orbital has degenerate electronic states. The calculated partial charge density is in line with the group theory analysis and defect-level calculations.

#### D. Tuning of defect levels by charge states

As aforementioned, even though the defect levels of  $P_S V_{Mg}$  split into spin-up and spin-down levels, the spin-up levels are fully filled with electrons, and the spin-down levels are empty. Therefore, the qubit center cannot be realized in the MgS semiconductor because there is no allowed optical transition since the spin state cannot be changed in a phonon line process. Thus, the  $P_S V_{Mg}$  defect in different charge states has been further investigated to seek potential candidate qubits.

First, the formation energies of the  $P_S V_{Mg}$  defect in charge state  $q$  have been studied, which is defined in the formula in Eq. (4) in computational details [63,64]. The formation energies of the  $P_S V_{Mg}$  defect in all considered charge states are shown in Fig. 6, in which each line represents the formation energy of the  $P_S V_{Mg}$  defect in a specific charge state. Obviously, the formation energy depends on the charge state. The stable charge state has the lowest formation energy for a given Fermi level. It is evident from Fig. 6 that the cyan and blue lines cross at the Fermi level of 2.53 eV, indicating that the  $P_S V_{Mg}^{2+}$  charge state is energetically stable with the lowest formation energy compared with other charge states in the range of the Fermi level from 0 to 2.53 eV. However, when the Fermi level is 2.53 eV, the  $P_S V_{Mg}^{2-}$  charge state becomes stable with the sufficiently low formation energy. It should be noted that the neutral  $P_S V_{Mg}$  defect center has significantly higher formation energy than other charge states, suggesting that an investigation limited only to neutral charge states would not produce a comprehensive picture of defect formation. In

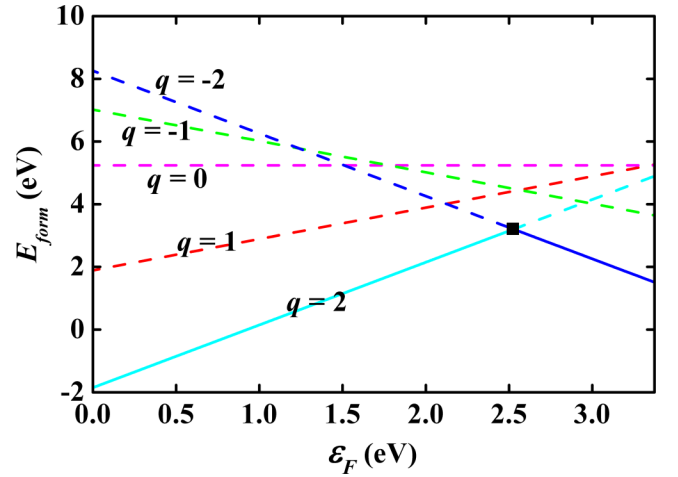


FIG. 6. The calculated defect formation energy of the  $P_S V_{Mg}$  defect center in different charge states as a function of Fermi levels.

addition, we performed test calculations for the formation energy of the  $P_S V_{Mg}$  defect center in different charge states as a function of Fermi levels in a supercell with 512 atoms. As shown in Fig. S5 in the Supplemental Material [59], with the Fermi level varying from the VBM to the CBM, the most stable charge state of the  $P_S V_{Mg}$  defect exhibits the  $P_S V_{Mg}^{2+}$  and  $P_S V_{Mg}^{2-}$  states; with transition of  $2/-2$ , the corresponding charge transition level is 2.96 eV. Therefore, all calculations in this paper were carried out using the  $2 \times 2 \times 2$  MgS supercell with 64 atoms since the large-sized supercells (e.g., the  $4 \times 4 \times 4$  MgS supercell with 512 atoms) are computationally too expensive, and the results are comparable with those in a 64-atom supercell.

Figure 7 shows the schematic diagram of defect levels in different charge states. In the  $q = +1$  charge state, an electron is ionized out of the highest occupied  $E_1^\uparrow$  level, and thus, the  $E_1^\uparrow$  level is empty. Thus, an electron can be excited from the  $E_y^\uparrow$  into the  $E_1^\uparrow$  level, resulting in the triplet ground state with the net spin of  $S = 1$  and the local magnetic moment of  $2 \mu_B$ . At the same time, the degenerate energy levels of spin-up states  $E_{xy}^\uparrow$  are relieved, and the single level of spin-down state  $E_1^\downarrow$  shifts up. For the case of  $q = +2$  charge state, the  $E_y^\uparrow$  level becomes empty as another electron is removed for the spin-up channel. This results in a doublet ground state with the net spin of  $S = \frac{1}{2}$  and the local magnetic moment of  $1 \mu_B$ . In this case, an electron can be excited from the  $E_x^\uparrow$  into the  $E_y^\uparrow$  level. Meanwhile, the degenerate levels of spin-down states  $E_{xy}^\downarrow$  relieve, and the relieved  $E_y^\downarrow$  level shifts up. In contrast to the positive charge states, in the  $q = -1$  charge state, the degenerate energy levels of spin-down states  $E_{xy}^\downarrow$  are relieved, and the relieved level  $E_x^\downarrow$  falls below the Fermi level owing to an additional electron occupying. This leads to the spin  $S = 1$  configuration and then the triplet ground state with the local magnetic moment of  $2 \mu_B$ , and thus, an occupied electron can be also excited from the  $E_x^\downarrow$  into the  $E_y^\downarrow$  level. When it is further charged to  $P_S V_{Mg}^{2-}$ , the other relieved level  $E_y^\downarrow$  also falls below the Fermi level, resulting in the net spin of  $S = \frac{1}{2}$  and the local magnetic moment of  $1 \mu_B$ . Then the  $E_{xy}^\downarrow$  levels

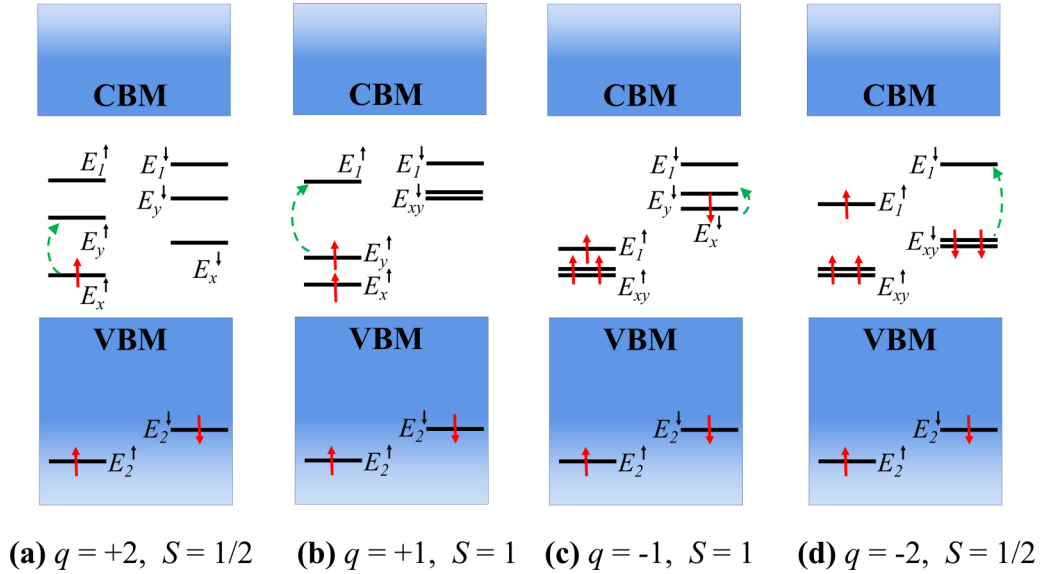


FIG. 7. The schematic diagram of the defect levels in the  $P_S V_{Mg}$  center in different charge states.  $q$  and  $S$  represent the charge state and net spin, respectively. The red arrow represents the occupied states, and the green arrow represents the electron transition. The two channels of spin-up and spin-down states are marked by up and down arrows, respectively.

are degenerate occupied, and the  $E_1^\downarrow$  level is empty. Thus, an occupied electron can be excited from the  $E_{xy}^\downarrow$  into the  $E_1^\downarrow$  level for the spin-down channel. Overall, the net spin and the position of defect levels in the bandgap can be tuned by changing the charge state of the  $P_S V_{Mg}$  defect. The four charged defects of  $P_S V_{Mg}^+$ ,  $P_S V_{Mg}^{2+}$ ,  $P_S V_{Mg}^-$ , and  $P_S V_{Mg}^{2-}$  thus may be potential candidate qubits. The energy band structures of the  $P_S V_{Mg}$  defect in different charge states calculated by first principles are shown in Fig. S6 in the Supplemental Material [59].

One of the most important quantities that can be obtained from first-principles calculation is the energy difference. Here, for the sake of convenience, we defined the energy difference in the same spin channel between the CBM and the lowest unoccupied defect level ( $E_{LUDL}$ ) as  $\Delta E_1$ , between the highest occupied defect level ( $E_{HODL}$ ) and the VBM as  $\Delta E_2$ , and the value of  $E_{LUDL}$  minus  $E_{HODL}$  is defined as  $\Delta E$ . The calculated values of  $\Delta E_1$ ,  $\Delta E_2$ , and  $\Delta E$  for four different charge states at the PBE and HSE levels are listed in Tables S1 and S2 in the Supplemental Material [59], respectively, from which we can see that the values of  $\Delta E$  for the relatively stable charge states ( $q = \pm 2$ ) are large enough to avoid the electron transition caused by thermal excitation. Unfortunately, the values of  $\Delta E_1$  and  $\Delta E_2$  for the  $P_S V_{Mg}^{2+}$  and  $P_S V_{Mg}^{2-}$  defects are smaller than the corresponding values of  $\Delta E$ , which is likely to introduce the interference of the electronic state from the host materials.

### E. Optical characteristics

To provide certain guidance for the optical excitation transitions in qubit materials, the ZPL, optical emission/absorption, Stokes shift, and anti-Stokes shift of the  $P_S V_{Mg}$  defect in various charge states were calculated; the configuration coordinate diagram is shown in Fig. 8, and the values are summarized in Table II. As shown in Fig. 8, the blue and green arrows represent the absorbing and emitting

processes of photons, respectively. Since the time of electron excitation or de-excitation is very short relative to the lattice relaxation, the corresponding structure remains in the ground or excited state. The ZPL equals the energy of the optimized excited state minus that of the optimized ground state, represented by the red arrow. Table II shows that the ZPLs are 0.78, 0.86, 0.27, and 0.88 eV for the charge states of +2, +1, -1, and -2, respectively. The corresponding fluorescence wavelengths are 1593.8, 1450.3, 4592.6, and 1407.5 nm, which are the infrared band. For the case of  $q = -1$ , if it is an allowable process, it may lead to sharp transition in the luminescence.

For the four charged defects such as  $P_S V_{Mg}^+$ ,  $P_S V_{Mg}^{2+}$ ,  $P_S V_{Mg}^-$ , and  $P_S V_{Mg}^{2-}$ , the concerned optical transitions are allowed. For example, in a charge state of  $q = -2$ , the system

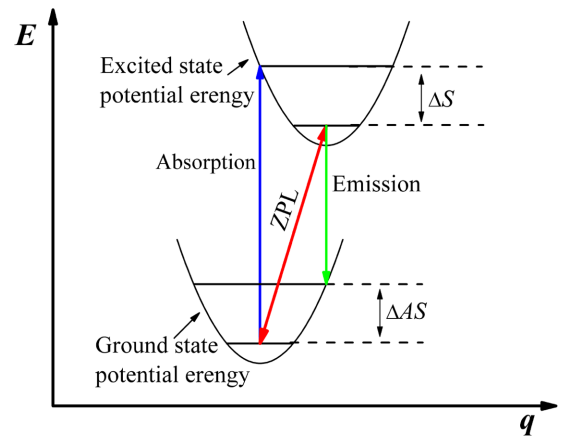


FIG. 8. The configuration coordinate diagram.  $E$  and  $q$  represent the total energy and the configuration coordinate, respectively. The blue and green arrows represent vertical absorption and vertical emission, respectively, and the red arrow is the zero-phonon line (ZPL).  $\Delta S$  and  $\Delta AS$  stand for Stokes shift and anti-Stokes shift, respectively.

TABLE II. The vertical absorption/emission, the ZPL, the Stokes shift, and the anti-Stokes shift of the  $V_{Mg}P_S$  defect center in various charge states (units in eV).

	Vertical absorption	Vertical emission	ZPL	$\Delta S$	$\Delta AS$
$P_S V_{Mg}^{2+}$	1.87	0.05	0.78	1.10	0.72
$P_S V_{Mg}^{+}$	2.02	0.30	0.86	1.16	0.55
$P_S V_{Mg}^{-}$	0.39	0.12	0.27	0.12	0.15
$P_S V_{Mg}^{2-}$	1.37	0.30	0.88	0.49	0.58

has  $C_{3v}$  symmetry and possesses a spin of  $S = \frac{1}{2}$ . In this system, according to the group theory, the occupied  $E_{xy}^{\downarrow}$  levels are degenerate, which are assigned to the irreducible representation of  $E$ , and the unoccupied  $E_1^{\downarrow}$  level to  $A_1$ . There is an electric dipole transition between  $E$  and  $A_1$ . Therefore, an electron can be excited from the  $E_{xy}^{\downarrow}$  level to the  $E_1^{\downarrow}$  level, as shown in Fig. 9 below.

Zero field splitting (ZFS) is another important parameter for qubit applications. For example, the electron spin of the defect center with the spin triplet can be effectively manipulated by microwaves, and the manipulation parameter is ZFS. ZFS is a splitting between the degenerate electron spin sub-levels for the system of  $S \geq 1$  without an external electric field, which is caused by the electron spin-spin dipole interaction. ZFS has two parameters in the eigenvalue framework; one is axial ZFS parameter  $D$ , the other is transverse ZFS parameter  $E$ , which are expressed by the diagonal elements of the tensor as [65]

$$D = \frac{3}{2}D_{zz}, \quad (12)$$

and

$$E = \frac{D_{yy} - D_{xx}}{2}. \quad (13)$$

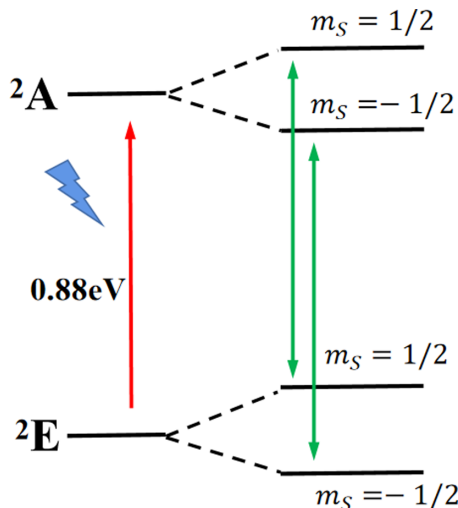


FIG. 9. Schematic diagram about energy levels of the  $P_S V_{Mg}^{2-}$  defect.

The ZFSs of the  $P_S V_{Mg}$  defect pair in  $+1$  and  $-1$  charge states were calculated, respectively. As a result, for the  $P_S V_{Mg}^{+}$  defect,  $D$  and  $E$  are  $1103.4$  and  $-1082.9$  MHz, respectively, and for the  $P_S V_{Mg}^{-}$  defect,  $D$  and  $E$  are  $-1851.9$  and  $1635.1$  MHz, respectively. The values of  $D$  are obviously in the range of microwaves, while the values of  $E$  are nonzero, perhaps because the defects are not strict  $C_{3v}$  symmetry.

## F. Hyperfine parameters

It should be noted that the background of the nuclear spin usually causes decoherence of electron spin bits. In our systems, although the nuclear spins of  $^{24}Mg$  and  $^{32}S$  are zero,  $^{25}Mg$  (with natural abundance of 10.11%),  $^{33}S$  (0.75%), and  $^{31}P$  (100%) have nonzero nuclear spins of  $\frac{5}{2}$ ,  $\frac{3}{2}$ , and  $\frac{1}{2}$ , respectively, which can cause hyperfine interaction between electron and nuclear spins. Therefore, it is necessary to calculate the hyperfine parameters for the  $P_S V_{Mg}$  defect pair in MgS crystal to estimate the hyperfine interaction intensity. The hyperfine interaction tensor can be used to describe the coupling of nuclear spin with the electron spin of the point defect. Generally, the hyperfine interaction spin Hamiltonian of a single pair of electron and nuclear spins can be written as

$$H_{\text{hyp}} = \hat{S} \hat{A} \hat{I}, \quad (14)$$

where  $A$  is the hyperfine interaction tensor, and  $\hat{S}$  and  $\hat{I}$  are the electronic and nuclear spin operators, respectively. When the electron spin density is nonzero at the place of the considered nuclear spin, the hyperfine interaction tensor elements are written as the sum of an isotropic part (Fermi contact term) and an anisotropic part (dipolar coupling term). The Fermi contact term is given by

$$(A_{\text{iso}})_{ij} = \frac{2\mu_0}{3} \frac{\gamma_e \gamma_I}{\langle S_Z \rangle} \delta_{ij} \int \delta_T(\vec{r}) \rho_s(\vec{r} + \vec{R}_I) d\vec{r}, \quad (15)$$

where  $\mu_0$  is the magnetic susceptibility of free space, and  $\gamma_e$  and  $\gamma_I$  are the electron gyromagnetic ratio and the nuclear gyromagnetic ratio, respectively. Here,  $\langle S_Z \rangle$  represents the expectation value of the  $z$  component of the total electronic spin. Also,  $\rho_s$  is the electron spin density, and  $\delta_T(\vec{r})$  is a smeared-out  $\delta$  function, as described in Ref. [66]. The dipolar contribution is given by

$$(A_{\text{ani}})_{ij} = \frac{\mu_0}{4\pi} \frac{\gamma_e \gamma_I}{\langle S_Z \rangle} \int \frac{3r_i r_j - \delta_{ij} r^2}{r^5} \rho_s(\vec{r} + \vec{R}_I) d\vec{r}, \quad (16)$$

where  $r = |\vec{r}|$ ,  $r_i$  is the  $i$ th component of  $\vec{r}$ , and  $\vec{r}$  is the vector between the electron and nuclear spins at  $\vec{R}_I$ .

In general, if the nuclear spin is located on the symmetry axis of the defect, the hyperfine interaction tensor  $A$  is diagonal with diagonal elements  $A_{xx}$ ,  $A_{yy}$ , and  $A_{zz}$ , that is, the principal values of the hyperfine interaction tensor (hyperfine constants). The calculated principal values of the hyperfine interaction tensor for the first and second neighbors of the P site and the distance from the P site are listed in Table III. The schematic diagram of the local structure and the spin difference charge density defined as  $\Delta\rho_s = \rho_{\text{up}} - \rho_{\text{down}}$  of the  $P_S V_{Mg}$  defect pair in MgS [67] are shown in Fig. 10, respectively. Table III shows that the principal values of hyperfine interaction tensors of the P atom are the largest ( $\approx 10^3$ )

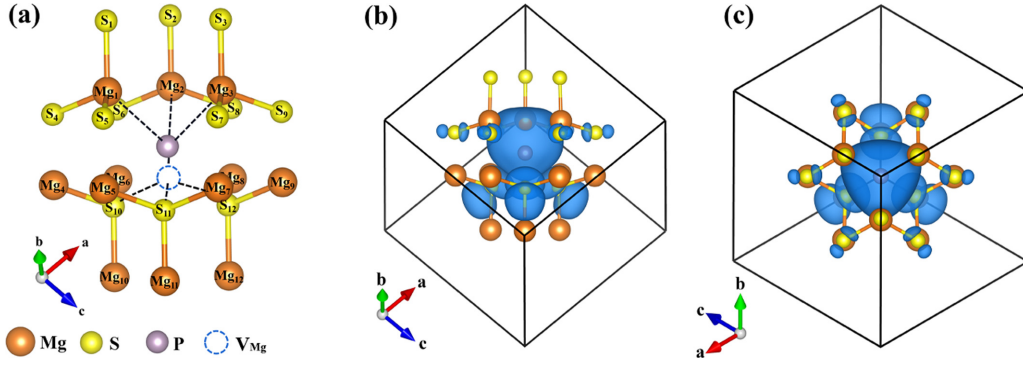


FIG. 10. Schematic diagram of (a) the local structure and (b) and (c) the spin difference charge density of the  $P_S V_{Mg}$  defect pair in MgS. We only show the atoms up to the second neighbors from the nucleus site; the isosurface value is  $1 \times 10^{-3} e/\text{\AA}^3$  for the spin difference charge density.

followed by the three nearest S atoms ( $\approx 10^2$ ), and the hyperfine constants of Mg atoms farther away from the P site further decrease ( $\approx 10^1$ ). Furthermore, the hyperfine interaction tensors of distant Mg and S atoms are small enough to ignore. These hyperfine constants are consistent with the spin difference charge density shown in Figs. 10(b) and 10(c), where the charge density is mainly localized on the P atom followed by the three nearest S ligands; very little charge density is localized on the six S atoms bonded to the Mg atoms, and it practically vanishes at distances larger than  $\sim 4.3$  \AA from the P site. The hyperfine constants are roughly proportional to the spin charge density and exponentially decay as a function of the distance from the P site. This trend is like the report by Wrachtrup *et al.* [68] based on their *ab initio* studies of the  $NV^-$  center in diamond. On the other hand, the Fermi contact term  $a$  and the dipolar coupling term  $b$  can be estimated by the formulas  $a = \frac{1}{3}(A_{xx} + A_{yy} + A_{zz})$  and  $b = \frac{1}{3}|\frac{A_{xx}+A_{yy}}{2} - A_{zz}|$ , respectively [62]. The hyperfine field is isotropic when  $b = 0$ . On the contrary, it is anisotropic when  $b \neq 0$ . Evidently, the hyperfine field of the  $P_S V_{Mg}$  defect in MgS is anisotropic.

In addition, we calculated the principal values of the hyperfine interaction tensor of the  $P_S V_{Mg}$  defect in the  $\pm 1$ ,  $\pm 2$  charge states, see Tables S3–S6 in the Supplemental Material [59]. The absolute values of the hyperfine parameters calculated from first principles can be directly compared with

TABLE III. The calculated principal values of the hyperfine interaction tensor ( $A_{xx}$ ,  $A_{yy}$ , and  $A_{zz}$ ) of the  $P_S V_{Mg}$  defect pair in MgS for the first and second neighbor of the P site (in MHz) and the distance ( $R_P$ ) from the P site (in \AA).

Atom	$R_P$	$A_{xx}$	$A_{yy}$	$A_{zz}$
P	0.00	347.67	287.21	347.67
$S_{10}, S_{11}, S_{12}$	2.96	15.82	15.54	36.36
$Mg_1, Mg_2, Mg_3$	3.01	-4.11	-4.08	-5.76
$S_1, S_2, S_3$	4.89	0.42	0.40	1.49
$S_4, S_5, S_6, S_7, S_8, S_9$	4.21	0.65	0.61	2.89
$Mg_{10}, Mg_{11}, Mg_{12}$	4.96	-1.38	-1.37	-1.82
$Mg_4, Mg_5, Mg_6, Mg_7, Mg_8, Mg_9$	4.20	0.26	0.22	0.34

the quantities measured by electron paramagnetic resonance (EPR). Currently, no experimental hyperfine data are available for the  $P_S V_{Mg}$  defect in different charge states. We expect that the calculated principal values of hyperfine interaction tensors in this paper will be compared with the experimental measurements by EPR in the future, and they can be used to further support the identification presented in this paper.

#### IV. SUMMARY AND CONCLUSIONS

In this paper, we attempt to seek potential candidate qubits in MgS host materials using first-principles calculations. Results show that the MgS semiconductor is suitable as a qubit host material with the wide bandgap, approximate zero nuclear spin, and weak SOC. Among the considered nine single point defects, the  $P_S$  and  $As_S$  point defects may be potential candidate qubits due to their reasonable defect levels. Furthermore, the defect pair of  $P_S V_{Mg}$  has been systematically studied. Both first-principles calculations and group theory analysis indicate that the defect-level sequence of neutral  $P_S V_{Mg}$  is  $E_1 > E_{exy} > E_2$ . In addition, the net spin and defect levels of  $P_S V_{Mg}$  can be tuned by charge states. With the Fermi level varying from the VBM to the CBM, the formation energy indicates that  $P_S V_{Mg}^{2+}$  and  $P_S V_{Mg}^{2-}$  are relatively stable charge states with the charge transition level of  $\sim 2.53$  eV. From the analysis of defect levels in  $P_S V_{Mg}^+$ ,  $P_S V_{Mg}^{2+}$ ,  $P_S V_{Mg}^-$ , and  $P_S V_{Mg}^{2-}$ , these four charged states may be plausible qubit candidates. Moreover, the ZPLs of  $P_S V_{Mg}$  in different charge states have been calculated, and the corresponding fluorescence wavelengths fall within the infrared band. The ZFSs of  $P_S V_{Mg}^+$  and  $P_S V_{Mg}^-$  show that the values of parameter  $D$  are in the range of microwaves, and then the electron spin of these defects can be effectively manipulated by microwaves. Finally, the principal values of the hyperfine tensor for the first and second neighbors of the P site and the spin difference charge density have been calculated. The results reveal that the spin difference charge density is mainly localized on the P atom followed by the three nearest S ligands. The hyperfine constants are roughly proportional to the spin difference charge density and exponentially decay as a function of the distance from the P site.



In summary, we have made a preliminary study on the qubits in defect MgS from the perspective of theoretical calculations. There are still many issues to be solved such as manipulation and measurement for the electron spin of the  $P_S V_{Mg}^{2+}$  and  $P_S V_{Mg}^{2-}$  defects, which need further research in theory and experiment and a deep physical understanding for the properties of qubits in the future.

## ACKNOWLEDGMENTS

This paper is supported by the Natural Science Foundation of China (Grant No. 12164020) and the Natural Science Foundation of Jiangxi Province, China (Grant No. 20202BAB201012). We gratefully acknowledge Hefei Advanced Computing Center for computational support.

- [1] V. Ivady, I. A. Abrikosov, and A. Gali, *npj Comput. Mater.* **4**, 76 (2018).
- [2] J. Davidsson, V. Ivády, R. Armiento, N. T. Son, A. Gali, and I. A. Abrikosov, *New J. Phys.* **20**, 023035 (2018).
- [3] S. Yang, Y. Wang, D. D. Bhaktavatsala Rao, T. H. Tran, A. S. Momenzadeh, M. Markham, D. J. Twitchen, P. Wang, W. Yang, R. Stöhr *et al.*, *Nat. Photonics* **10**, 507 (2016).
- [4] N. Kalb, A. A. Reiserer, P. C. Humphreys, J. J. W. Bakermans, S. J. Kamerling, N. H. Nickerson, S. C. Benjamin, D. J. Twitchen, M. Markham, and R. Hanson, *Science* **356**, 928 (2017).
- [5] C. Monroe, R. Raussendorf, A. Ruthven, K. R. Brown, P. Maunz, L. M. Duan, and J. Kim, *Phys. Rev. A* **89**, 022317 (2014).
- [6] N. H. Nickerson, Y. Li, and S. C. Benjamin, *Nat. Commun.* **4**, 1756 (2013).
- [7] J. Cramer, N. Kalb, M. A. Rol, B. Hensen, M. S. Blok, M. Markham, D. J. Twitchen, R. Hanson, and T. H. Taminiau, *Nat. Commun.* **7**, 11526 (2016).
- [8] J. Cai, A. Retzker, F. Jelezko, and M. B. Plenio, *Nat. Phys.* **9**, 168 (2013).
- [9] D. D. Awschalom, L. C. Bassett, A. S. Dzurak, E. L. Hu, and J. R. Petta, *Science* **339**, 1174 (2013).
- [10] M. Pfender, N. Aslam, H. Sumiya, S. Onoda, P. Neumann, J. Isoya, C. A. Meriles, and J. Wrachtrup, *Nat. Commun.* **8**, 834 (2017).
- [11] D. R. Glenn, D. B. Bucher, J. Lee, M. D. Lukin, H. Park, and R. L. Walsworth, *Nature (London)* **555**, 351 (2018).
- [12] H. Kraus, V. A. Soltamov, F. Fuchs, D. Simin, A. Sperlich, P. G. Baranov, G. V. Astakhov, and V. Dyakonov, *Sci. Rep.* **4**, 5303 (2014).
- [13] G. Kucsko, P. C. Maurer, N. Y. Yao, M. Kubo, H. J. Noh, P. K. Lo, H. Park, and M. D. Lukin, *Nature (London)* **500**, 54 (2013).
- [14] T. Iwasaki, W. Naruki, K. Tahara, T. Makino, H. Kato, M. Ogura, D. Takeuchi, S. Yamasaki, and M. Hatano, *ACS Nano* **11**, 1238 (2017).
- [15] M. S. J. Barson, P. Peddibhotla, P. Ovarthaiyapong, K. Ganesan, R. L. Taylor, M. Gebert, Z. Mielens, B. Koslowski, D. A. Simpson, L. P. McGuinness *et al.*, *Nano Lett.* **17**, 1496 (2017).
- [16] S. Castelletto, B. C. Johnson, V. Ivady, N. Stavrias, T. Umeda, A. Gali, and T. Ohshima, *Nat. Mater.* **13**, 151 (2014).
- [17] I. Aharonovich, D. Englund, and M. Toth, *Nat. Photonics* **10**, 631 (2016).
- [18] F. Jelezko and J. Wrachtrup, *Phys. Status Solidi A* **203**, 3207 (2006).
- [19] R. Hanson and D. D. Awschalom, *Nature (London)* **453**, 1043 (2008).
- [20] F. Jelezko, T. Gaebel, I. Popa, A. Gruber, and J. Wrachtrup, *Phys. Rev. Lett.* **92**, 076401 (2004).
- [21] D. D. Awschalom and M. E. Flatté, *Nat. Phys.* **3**, 153 (2007).
- [22] J. Riedrich-Möller, L. Kipfstuhl, C. Hepp, E. Neu, C. Pauly, F. Mücklich, A. Baur, M. Wandt, S. Wolff, M. Fischer, S. Gsell, M. Schreck, and C. Becher, *Nat. Nanotechnol.* **7**, 69 (2012).
- [23] E. Neu, D. Steinmetz, J. Riedrich-Moeller, S. Gsell, M. Fischer, M. Schreck, and C. Becher, *New J. Phys.* **13**, 025012 (2011).
- [24] A. Sipahigil, K. D. Jahnke, L. J. Rogers, T. Teraji, J. Isoya, A. S. Zibrov, F. Jelezko, and M. D. Lukin, *Phys. Rev. Lett.* **113**, 113602 (2014).
- [25] H. J. Kimble, *Nature (London)* **453**, 1023 (2008).
- [26] A. Sipahigil, R. E. Evans, D. D. Sukachev, M. J. Burek, J. Borregaard, M. K. Bhaskar, C. T. Nguyen, J. L. Pacheco, H. A. Atikian, C. Meuwly *et al.*, *Science* **354**, 847 (2016).
- [27] S. Johnson, P. R. Dolan, T. Grange, A. A. P. Trichet, G. Hornecker, Y. C. Chen, L. Weng, G. M. Hughes, A. A. R. Watt, A. Auffèves *et al.*, *New J. Phys.* **17**, 122003 (2015).
- [28] M. Hanks, M. Trupke, J. Schmiedmayer, W. J. Munro, and K. Nemoto, *New J. Phys.* **19**, 103002 (2017).
- [29] Á. Gali, *Nanophotonics* **8**, 1907 (2019).
- [30] A. Gali and J. R. Maze, *Phys. Rev. B* **88**, 235205 (2013).
- [31] C. Hepp, T. Müller, V. Waselowski, J. N. Becker, B. Pingault, H. Sternschulte, D. Steinmüller-Nethl, A. Gali, J. R. Maze, M. Atatüre *et al.*, *Phys. Rev. Lett.* **112**, 036405 (2014).
- [32] L. J. Rogers, K. D. Jahnke, T. Teraji, L. Marseglia, C. Müller, B. Naydenov, H. Schauffert, C. Kranz, J. Isoya, L. P. McGuinness *et al.*, *Nat. Commun.* **5**, 4739 (2014).
- [33] B. Pingault, D.-D. Jarausch, C. Hepp, L. Klintberg, J. N. Becker, M. Markham, C. Becher, and M. Atatüre, *Nat. Commun.* **8**, 15579 (2017).
- [34] J. N. Becker and C. Becher, *Phys. Status Solidi A* **214**, 1700586 (2017).
- [35] B. C. Rose, D. Huang, Z.-H. Zhang, P. Stevenson, A. M. Tyryshkin, S. Sangtawesin, S. Srinivasan, L. Loudin, M. L. Markham, A. M. Edmonds *et al.*, *Science* **361**, 60 (2018).
- [36] M. K. Bhaskar, D. D. Sukachev, A. Sipahigil, R. E. Evans, M. J. Burek, C. T. Nguyen, L. J. Rogers, P. Siyushev, M. H. Metsch, H. Park *et al.*, *Phys. Rev. Lett.* **118**, 223603 (2017).
- [37] P. Siyushev, M. H. Metsch, A. Ijaz, J. M. Binder, M. K. Bhaskar, D. D. Sukachev, A. Sipahigil, R. E. Evans, C. T. Nguyen, M. D. Lukin *et al.*, *Phys. Rev. B* **96**, 081201(R) (2017).
- [38] T. Iwasaki, Y. Miyamoto, T. Taniguchi, P. Siyushev, M. H. Metsch, F. Jelezko, and M. Hatano, *Phys. Rev. Lett.* **119**, 253601 (2017).
- [39] F. Pan, M. Zhao, and L. Mei, *J. Appl. Phys.* **108**, 043917 (2010).
- [40] X. Wang, M. Zhao, H. Xia, S. Yan, and X. Liu, *J. Appl. Phys.* **110**, 033711 (2011).

- [41] W. F. Koehl, B. B. Buckley, F. J. Heremans, G. Calusine, and D. D. Awschalom, *Nature (London)* **479**, 84 (2011).
- [42] D. J. Christle, P. V. Klimov, C. F. de las Casas, K. Szász, V. Ivády, V. Jokubavicius, J. Ul Hassan, M. Syväjärvi, W. F. Koehl, T. Ohshima *et al.*, *Phys. Rev. X* **7**, 021046 (2017).
- [43] C. F. de las Casas, D. J. Christle, J. Ul Hassan, T. Ohshima, N. T. Son, and D. D. Awschalom, *Appl. Phys. Lett.* **111**, 262403 (2017).
- [44] J. C. Ribierre, A. Ruseckas, K. Knights, S. V. Staton, N. Cumpstey, P. L. Burn, and I. D. W. Samuel, *Phys. Rev. Lett.* **100**, 017402 (2008).
- [45] X. Wang, M. Zhao, Z. Wang, X. He, Y. Xi, and S. Yan, *Appl. Phys. Lett.* **100**, 192401 (2012).
- [46] R. Gao, G. Bian, H. Yuan, and H. Wang, *J. Phys. D: Appl. Phys.* **54**, 505109 (2021).
- [47] G. Bian, H. Yuan, N. Zhang, L. Xu, J. Zhang, P. Fan, H. Wang, C. Zhang, G. Shan, Q. Zhang *et al.*, *Appl. Phys. Lett.* **114**, 102105 (2019).
- [48] J. R. Weber, W. F. Koehl, J. B. Varley, A. Janotti, B. B. Buckley, C. G. Van de Walle, and D. D. Awschalom, *Proc. Natl. Acad. Sci. USA*. **107**, 8513 (2010).
- [49] J. R. Weber, W. F. Koehl, J. B. Varley, A. Janotti, B. B. Buckley, C. G. Van de Walle, and D. D. Awschalom, *J. Appl. Phys.* **109**, 102417 (2011).
- [50] G. Kresse and J. Hafner, *Phys. Rev. B* **47**, 558 (1993).
- [51] G. Kresse and J. Furthmüller, *Phys. Rev. B* **54**, 11169 (1996).
- [52] G. Kresse and D. Joubert, *Phys. Rev. B* **59**, 1758 (1999).
- [53] P. E. Blöchl, *Phys. Rev. B* **50**, 17953 (1994).
- [54] J. P. Perdew, K. Burke, and M. Ernzerhof, *Phys. Rev. Lett.* **77**, 3865 (1996).
- [55] A. Togo and I. Tanaka, *Scr. Mater.* **108**, 1 (2015).
- [56] H. J. Monkhorst and J. D. Pack, *Phys. Rev. B* **13**, 5188 (1976).
- [57] H. Okuyama, Y. Kishita, and A. Ishibashi, *Phys. Rev. B* **57**, 2257 (1998).
- [58] F. El Haj Hassan and B. Amrani, *J. Phys. Condens. Matter* **19**, 386234 (2007).
- [59] See Supplemental Material at <http://link.aps.org/supplemental/10.1103/PhysRevB.105.224104> for configurations and projected density of states of vacancy and impurity defects, test data in a supercell with 512 atoms, band structures of  $P_S V_{Mg}$  defect in different charge states, the energy difference, and the principal values of the hyperfine interaction tensor data.
- [60] F. M. Hossain, M. W. Doherty, H. F. Wilson, and L. C. L. Hollenberg, *Phys. Rev. Lett.* **101**, 226403 (2008).
- [61] T. Chanier, I. Opahle, M. Sargolzaei, R. Hayn, and M. Lannoo, *Phys. Rev. Lett.* **100**, 026405 (2008).
- [62] A. Gali, M. Fyta, and E. Kaxiras, *Phys. Rev. B* **77**, 155206 (2008).
- [63] P. Tuo and B. C. Pan, *Phys. Chem. Chem. Phys.* **21**, 5295 (2019).
- [64] C. G. Van de Walle and J. Neugebauer, *J. Appl. Phys.* **95**, 3851 (2004).
- [65] V. Ivády, T. Simon, J. R. Maze, I. A. Abrikosov, and A. Gali, *Phys. Rev. B* **90**, 235205 (2014).
- [66] P. E. Blöchl, *Phys. Rev. B* **62**, 6158 (2000).
- [67] A. Szállás, K. Szász, X. T. Trinh, N. T. Son, E. Jánzén, and A. Gali, *J. Appl. Phys.* **116**, 113702 (2014).
- [68] J. Wrachtrup, S. Y. Kilin, and A. P. Nizovtsev, *Opt. Spectrosc.* **91**, 429 (2014).